The Electrothermal Instability on Pulsed Power Ablations of Thin Foils

Adam M. Steiner, *Member, IEEE*, Paul C. Campbell, *Member, IEEE*, David A. Yager-Elorriaga, *Member, IEEE*, Nicholas M. Jordan, *Member, IEEE*, Ryan D. McBride, *Member, IEEE*, Y. Y. Lau, *Fellow, IEEE*, and Ronald M. Gilgenbach, *Life Fellow, IEEE*

***Abstract*— Presented are results from the optical imaging of atmospheric ablations of thin aluminum foils. These experiments were performed to evaluate the growth of temperature perturbations attributed to the electrothermal instability (ETI). ETI has been shown to seed magnetohydrodynamic instabilities on pulsed power-driven ablations of initially solid metallic targets, a topic of interest to various programs in pulsed power-driven plasma physics that depend on stable liner implosions. Experimental observations presented herein demonstrate exponentially growing temperature perturbations perpendicular to the direction of current with growth rates consistent with the linear ETI theory. High-temperature regions were observed to enter the vapor phase before sufficient energy had been deposited in the bulk foil to overcome the latent heat of vaporization, indicating a significant spatial heterogeneity in energy deposition rates. The growth rates of these perturbations scale as the square of current density, the predicted behavior for long-wavelength ETI structures. The development of these structures was unchanged by physical deformation of the foil surface, but dramatically influenced by incorporating areas of local high resistance in the foil loads. Extending the observation window in time showed a transition from perpendicular to parallel filaments, which is significant because ETI is predicted to switch orientations when the bulk foil material transitions into the plasma state. Collectively, these results provide an experimental validation of many theoretical predictions regarding ETI.**

***Index Terms*— Electrothermal effects, optical imaging, plasma pinch, plasma stability.**

Manuscript received March 12, 2018; revised July 16, 2018; accepted August 30, 2018. Date of publication October 25, 2018; date of current version November 8, 2018. This work was supported in part by DOE under Award DE-SC0012328, in part by NNSA through DOE Cooperative Agreement under Grant DE-NA0001984, in part by the Sandia National Laboratories under Contract DE-NA0003525, in part by the National Science Foundation under Grant PHY-1705418, and in part by DURIP, AFOSR under Grant #FA9550-15-1-0419. The work of D. A. Yager-Elorriaga was supported by an NSF Fellowship under Grant DGE-1256260. The review of this paper was arranged by Senior Editor F. Beg. *(Corresponding author: Adam M. Steiner.)*

A. M. Steiner was with the Department of Nuclear Engineering and Radiological Sciences, University of Michigan, Ann Arbor, MI 48109 USA. He is now with Lockheed Martin Aeronautics Company, Palmdale, CA 93599 USA (e-mail: amsteine@umich.edu).

P. C. Campbell, N. M. Jordan, R. D. McBride, Y. Y. Lau, and R. M. Gilgenbach are with the Department of Nuclear Engineering and Radiological Sciences, University of Michigan, Ann Arbor, MI 48109 USA.

D. A. Yager-Elorriaga was with the Department of Nuclear Engineering and Radiological Sciences, University of Michigan, Ann Arbor, MI 48109 USA. He is now with the Sandia National Laboratories, Albuquerque, NM 87185 USA.

Color versions of one or more of the figures in this paper are available online at http://ieeexplore.ieee.org.

Digital Object Identifier 10.1109/TPS.2018.2873947

I. Introduction

THE ablation of initially solid metals on pulsed power drivers is an active area of research with applications in dynamic material properties [1], [2], intense radiation generation [3]–[6], and magnetized liner inertial fusion [7]–[11]. These experiments typically seek to minimize the growth of magnetohydrodynamic (MHD) instabilities, such as the magneto-Rayleigh–Taylor (MRT) instability [11], [12], for optimum performance. Theoretical and experimental studies have provided significant evidence showing that the initial surface perturbations from which these instabilities grow can be seeded by a phenomenon known as the electrothermal instability (ETI) [13]–[17]. Therefore, controlling ETI may provide a means to reduce the impact of plasma instabilities on ablations of metallic targets.

ETI refers to the growth of a temperature perturbation in an ohmically heated medium with temperature-dependent resistivity $\eta(T)$. These temperature perturbations tend to manifest as striations of hot and cold material perpendicular to the flow of current when $\partial\eta/\partial T > 0$ (e.g., in condensed metals) and as filamentations parallel to the flow of current when $(\partial\eta/\partial T) < 0$ (e.g., in Spitzer-like plasma). A qualitative description of the mechanism believed to be responsible for the self-organization of initial perturbations into striations or filamentations (depending on the sign of $\partial\eta/\partial T$) is presented in Fig. 1.

The general linear dispersion relation for ETI [13], [18] in a thin foil or cylindrical liner of thickness d with current density J directed along the z-axis, neglecting the effects of material expansion, is given by

$$\gamma(t,T,k) = \frac{J_z^2 \frac{\partial\eta}{\partial T}\left(1 - \frac{\cos^2\alpha}{1+\left(\frac{\gamma}{\gamma_0}\right)}\right) - k^2\kappa}{\rho c_v}. \tag{1}$$

In (1), γ is the instantaneous growth rate of ETI as a function of time t, temperature T, and wavenumber $k = 2\pi/\lambda$; α is the angle between a perturbation and the z-axis (such that $\cos\alpha = 0$ when the wave vector is in the z-direction); κ, ρ, and c_v are the temperature-dependent thermal conductivity, density, and specific heat capacity of the unperturbed material; and γ_0 is a characteristic growth rate given

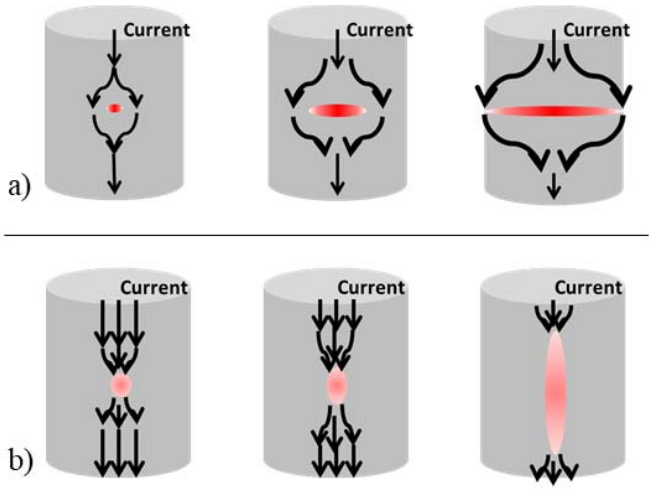

Fig. 1. Self-correlation of ETI on ohmically heated objects. (a) Striation form, $\partial\eta/\partial T > 0$: initial hotspots grow from nonuniformities in resistivity and increase in resistance as temperature rises due to locally increased Ohmic heating (left). Current density concentrates near the edges of the hotspot, which leads to areas of increased heating on either side of the hotspot (center), expanding the hotspot in the direction perpendicular to current until the hotspot has become a striation (right). (b) Filamentation form, $\partial\eta/\partial T < 0$: an initial hotspot is less resistive, which draws more current into the hotspot than the surrounding material (left). This causes areas of high current density above and below the hotspot, increasing the ohmic heating in these regions and expanding the hotspot vertically (center), continuing in the direction parallel to current until the hotspot has become a filament (right).

by

$$\gamma_0 = \frac{2k\eta}{\mu d} \tag{2}$$

where μ is the permeability of the material. The first term in (1) is the dominant growth term when $\partial\eta/\partial T > 0$, the second term is the dominant growth term when $\partial\eta/\partial T < 0$, and the third term describes damping due to thermal conductivity.

The growth of the $\partial\eta/\partial T > 0$ striation form of ETI is of particular interest to pulsed power plasma physics experiments, as these exponentially growing, perpendicular-to-current temperature perturbations cause sections of the initially solid metallic target to ablate before the bulk material. Surface perturbations arising from this process can provide the initial seed on the plasma–vacuum boundary from which MHD [19], [20] and MRT [11], [15], [16] instabilities can grow. When $\partial\eta/\partial T$ is positive, as is initially the case during a pulsed power ablation of a condensed metal target, the minimum growing ETI wavelength is given as

$$\lambda_{\min} = \frac{2\pi}{J}\sqrt{\kappa\left(\frac{\partial\eta}{\partial T}\right)^{-1}} \tag{3}$$

and the maximum growth rate, corresponding to $\cos\alpha = 0$, for a given wavelength is

$$\gamma_m(t,T,k) = \frac{\partial\eta}{\partial T}\frac{J^2}{\rho c_v} - \frac{k^2\kappa}{\rho c_v}. \tag{4}$$

For large wavelength perturbations, $\lambda = 2\pi/k \gg \lambda_{\min}$, the first term in (4) dominates, that is,

$$\gamma_{\max}(t,T) = \frac{\partial\eta}{\partial T}\frac{J^2}{\rho c_v}. \tag{5}$$

It is noteworthy that while $\partial\eta/\partial T$, ρ, and c_v are in general functions of temperature, for many metals, including aluminum, the ratio $(\partial\eta/\partial T)/\rho c_v$ is approximately constant over a large temperature range. (For liquid aluminum, this ratio varies from 3.3×10^{-17} $\mathrm{m}^4/(\mathrm{A}^2 \cdot \mathrm{s})$ to 3.8×10^{-17} $\mathrm{m}^4/(\mathrm{A}^2 \cdot \mathrm{s})$ between the melting and the vaporization points at atmospheric pressure [21]–[26].) Therefore, it is anticipated that large-wavelength ETI perturbations exhibit a growth rate that is approximately proportional to J^2 in such materials.

When $\partial\eta/\partial T$ is negative, which is expected to occur when the target has fully ablated and entered a plasma state exhibiting Spitzer-like resistivity, (1) is quadratic in γ, with the maximum growth rate corresponding to $\alpha = \pi/2$. Regardless of the sign of $\partial\eta/\partial T$, the manipulation of (1) also yields a condition on α:

$$\cos^2\alpha < \frac{1}{2}\left(1 - \frac{k^2\kappa}{J^2}\left(\frac{\partial\eta}{\partial T}\right)^{-1}\right). \tag{6}$$

Note that (1)–(6) are derived assuming that the current-carrying material does not expand. While this is a reasonable assumption for solids and liquids, the effects of material expansion may become important once the material reaches the vaporization point. The linear dispersion relation for perpendicular-to-current ETI structures in an expanding medium, derived in [27], is given by

$$\gamma = \frac{J^2\frac{\partial\eta}{\partial T} - k^2\kappa + \frac{\rho}{T^*}\left(c_v\frac{\partial T}{\partial t} - J^2\frac{\partial\eta}{\partial\rho}\right)}{\rho c_v + \frac{p}{T^*}}, \tag{7}$$

where p is pressure and T^* is a characteristic temperature established using a simplified equation of state. The first two terms in (7) are analogous to the expansion-free case in (4), the third term represents an additional destabilizing term arising from material heating, and the fourth term represents the increase in resistivity with decreasing density. These terms allow perpendicular-to-current ETI to continue to grow even after the material has transitioned into the plasma state until $\partial\eta/\partial T$ becomes sufficiently negative to overcome the additional growth terms.

Previous experimental work by Awe *et al.* [28] demonstrated the growth of bright, hot regions on pulsed power ablations of electrically thick (physical size greater than skin depth δ), cylindrical rods. The Awe *et al.* study demonstrated the self-organization of initial resistivity perturbations into perpendicular-to-current striations (as in Fig. 1); additionally, the transition to parallel-to-current filamentations was observed after the rod surface ablated [28].

In the present work, we establish a procedure for estimating the position-dependent temperature of ablating, ultrathin (0.4 to 2.0 μm thickness) aluminum foils from light emission observed on an ultrafast intensified charge-coupled device (ICCD) camera. By choosing a geometry that is electrically thin (thickness $\ll \delta$), we restrict the generally 3-D process of current division to two dimensions, allowing for more direct comparison with linear ETI theory summarized in (1)–(7). In addition, correlating light emission to temperature allows for a direct comparison of experimental and predicted ETI growth rates.

Our experimental setup is described in Section II. Section III details the procedure employed to estimate position-dependent temperature from light emission observed on the ICCD. In Section IV, we present 12-frame temperature measurements of ablating aluminum foils, demonstrating physics consistent with the theory of ETI. Section V presents a growth rate analysis of the experimentally measured temperature perturbations. Our results and analysis yield the following four key observations: 1) ablations of thin metallic liners demonstrated exponentially growing temperature perturbations perpendicular to the direction of current flow prior to the bulk material entering the plasma phase; 2) the growth rate of large-wavelength perturbations scaled with J^2, the predicted ETI behavior; 3) the seeding of these perturbations was unchanged by the physical deformation of the foil surface, but dramatically influenced by including areas of local high resistance; and 4) extending the observation window showed a transition from perpendicular striations of a hotter material to parallel filaments of the hotter material. Our conclusions are summarized in Section VI.

II. Experimental Setup

Ablations of thin planar foils in ambient, atmospheric pressure air were carried out on a pulse generator consisting of a single 240-nF capacitor in series with a self-breaking spark gap switch which closes at an applied voltage of 13 kV. HV-insulated wires connecting the pulse generator to the load have an equivalent inductance of 864 nH, and a resistor array totaling 0.83 Ω is connected in series to the output of the switch. This relatively large impedance (along with the equivalent series resistance and inductance of the switch and capacitor of 0.28 Ω and 80 nH) leads to a pulse of 4-kA peak current and a 600-ns rise time that is load-independent to within 5% for all foil loads used in these experiments. A schematic of the pulse generator/load circuit is shown in Fig. 2(a).

The load current density was varied between shots by changing the dimensions of the foil loads. The experiments described in this paper utilized Goodfellow aluminum foils of thicknesses 400 nm, 800 nm, and 2.0 μm. These foils are of 99.1% rated purity, with impurities primarily consisting of iron (0.47%), silicon (0.16%), titanium (0.07%), and gallium (0.05%). Foils were cut into strips of length 15 mm with widths varying from 2.5 to 10 mm using a razor edge. This variance of thickness and width allowed the investigation of a peak current density parameter space of approximately 2×10^7 A/cm^2 to 4×10^8 A/cm^2. A manufacturer-specified uncertainty on foil thickness of 25%, along with an estimated cutting width uncertainty of 10%, and places an uncertainty of 27% on the current density. The thickness uncertainty is due to the rolling process used to generate the thin foils, which introduces perturbations of much longer characteristic length scale than the dimensions of the foils used in these experiments. In addition, the examination of the razor-cut foil edges under an optical microscope showed edge fraying on the order of $\sim$10 μm (less than 1% of the foil widths used in these experiments). Therefore, we apply a 27% uncertainty to current density on a shot-to-shot basis, but we estimate spatial current density variation over a given shot to be on the order of a few percent.

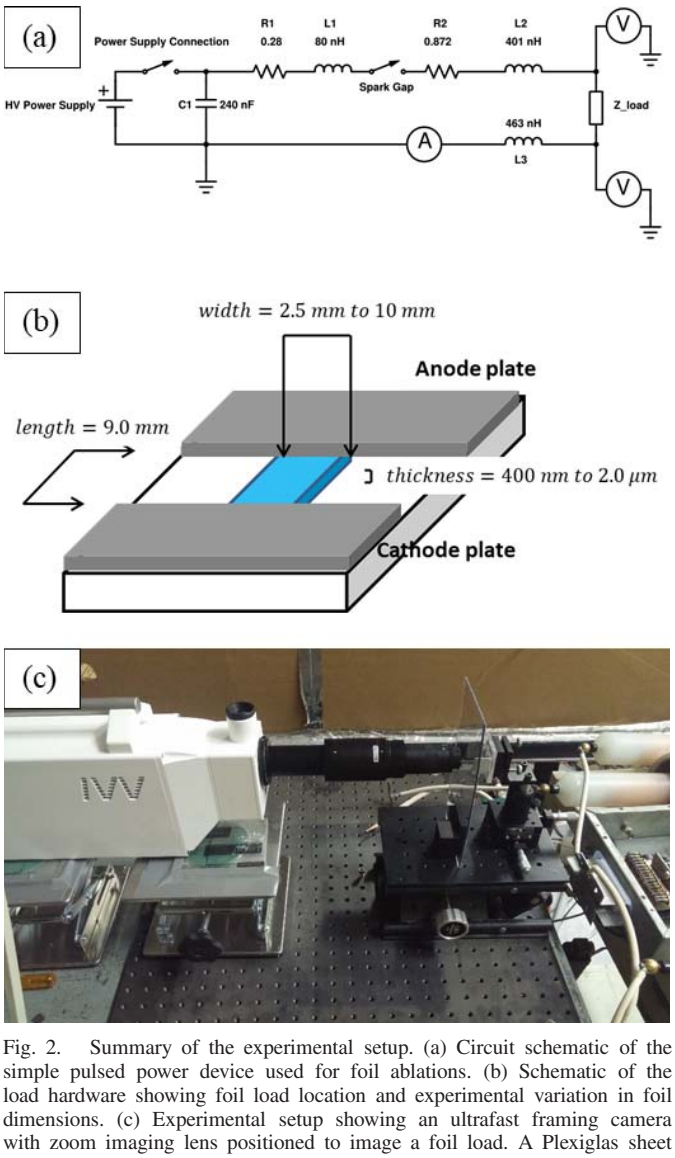

Fig. 2. Summary of the experimental setup. (a) Circuit schematic of the simple pulsed power device used for foil ablations. (b) Schematic of the load hardware showing foil load location and experimental variation in foil dimensions. (c) Experimental setup showing an ultrafast framing camera with zoom imaging lens positioned to image a foil load. A Plexiglas sheet positioned between the load and the imaging lens prevents debris from the exploding foil from damaging the lens.

The load hardware consisted of two aluminum plates connected to the anode and cathode of the pulse generator which were spaced 9 mm apart and mounted on a plastic support structure. For each shot, foils were cut and placed on the support structure; the load hardware plates were secured on top of the foil to provide electrical contact [see Fig. 2(b)]. The assembled load hardware was affixed to optical stands and placed on an array of translation stages to allow controlled movement in the x-, y-, and z-directions. Time-dependent load current and voltage were measured using a Pearson Electronics wideband current monitor and two ground-referenced North Star PVM-5 high-voltage probes connected to the anode and cathode plates. These diagnostics allowed for time-resolved measurements of power delivered to the load.

The primary optical diagnostic fielded in these experiments was a 12-frame, ultrafast, ICCD camera produced by Invisible Vision. The maximum frame rate of this camera is 2×10^8

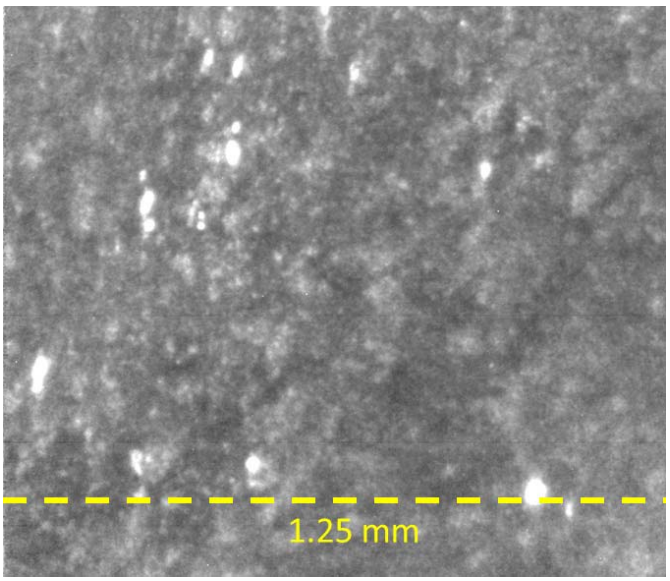

Fig. 3. Preshot image showing typical foil surface characteristics. Bright spots are due to a combination of sharp points on the surface of the foil resulting from folds and impurity inclusions of differing reflectance.

frames per second, and the minimum exposure time per frame is 5 ns. An Edmund Optics VZM-1000 Zoom Imaging Lens was mounted on the camera to provide optical magnification ranging from 2.5 to 10 [see Fig. 2(c)]. A backlit 1951 USAF resolution test target positioned at the in-focus imaging distance for the maximum 10× magnification yielded a minimum resolvable wavelength of 2.5 μm (400 line pairs/mm).

The framing camera was used to collect self-emission in the visible portion of the spectrum from the ablating foils as a function of time. A response versus wavelength curve supplied by the manufacturer was used for the calibration procedure described in Section III. Several shots utilized time-integrated spectroscopy to obtain information about the composition of plasma formed during foil ablation. The Acton SP-750i spectrometer fielded on these shots was calibrated *in situ* for absolute irradiance using a 40-W, OL-245 standard of spectral irradiance; wavelength-shift calibration was performed using neon, argon, and mercury lamps positioned at the location of the load hardware.

For each shot, the translation stages were used to make fine adjustments to load position to optimize focus and to fix the camera imaging window on the center of the foil, which was maintained as the region of interest to minimize the contribution of edge effects such as contact resistance with the electrodes. Each foil was imaged *in situ* prior to the shot using a long (∼10 ms) exposure setting on the framing camera and illuminating the surface of the foil with a high-intensity LED flashlight. Microscopic foil nonuniformities including wrinkles and impurity inclusions are visible on these preshot images (see Fig. 3).

III. Procedure for Estimating Material Temperature

To allow observation of ETI as a perturbation in temperature (as opposed to a physical boundary perturbation characteristic of most plasma instabilities), it was necessary to develop a method to correlate the time-resolved light emission measurements on the framing camera with instantaneous surface temperature. Graybody thermal radiation was assumed to be the dominant mechanism responsible for the self-emission detected by the camera as the foil material transitioned through the liquid, vapor, and weakly ionized plasma states. (Note that because the minimum resolvable emission using this diagnostic corresponded to a surface temperature of ∼2500 K, no emission was observable while the foil material was in the solid state.) To support this assumption, the contributions from competing mechanisms of line emission, Bremsstrahlung radiation, and radiative recombination/free-bound transmission emission were considered and found to be no more than a few percent of the total observed visible spectrum radiation. These calculations employed conservative estimates of electron temperature and number density, applied late into the current pulse after most of the capacitively stored energy has been deposited into the ablating foil. Details of these calculations can be found in [29].

Bright striations of the hotter material were consistently observed on aluminum foil ablations; the dynamics of these striations are addressed in Section IV. The time-integrated spectroscopic analysis of emitted light from these ablations consistently showed 466-nm lines attributed to Al-II superimposed onto a blackbody emission curve. Varying the background gas by conducting the ablation within a transparent plastic enclosure and flowing N_2, Ar, or SF_6 fill gases did not alter the measured spectra, and no lines attributable to the background gas were visible on any shots on which spectroscopy was fielded (the effects of surface contaminants, such as hydrocarbons, were not considered in this paper). Conducting ablations on a similar setup in vacuum resulted in substantially lower total emission levels. The observed dynamics of emitting features were qualitatively similar between air, N_2, and Ar, but emitting features expanded noticeably slower in SF_6. Quantitative changes in dynamics of the ablating features due to different background gases were considered outside the scope of this paper. We interpret these results to indicate: 1) the source of the light emission was weakly ionized aluminum, not the background gas and 2) the presence of ambient pressure slowed the expansion of vaporized aluminum (compared to its velocity in a vacuum) to the medium-dependent shock velocity [30], [31]. The presence of non-zero ambient pressure caused sections of the aluminum which have entered the vapor phase to remain in good electrical contact with the bulk material longer for ablations in the air compared to ablations in a vacuum. For this reason, atmospheric pressure ablations provide a longer timescale to observe ETI, allowing a more electrical energy to be deposited into these regions before they disperse explosively. All ablations analyzed in this paper were performed in ambient, atmospheric pressure air.

With the assumptions that light emission originates from the ablating foil material and behaves as a graybody, the temperature can be computed from the camera response, which is linear with incident irradiance at values below saturation according to manufacturer specifications. This calibration is accomplished by determining the integral radiated power for

a graybody source of given temperature, image size, and emissivity; adjusting for the wavelength-dependent response of the camera; and calibrating against a graybody source of the known temperature and emissivity. This process provides a 12-frame temperature imaging with the same spatial and temporal resolution as the framing camera system.

To calibrate the camera response, a tungsten standard of spectral irradiance (emissivity 0.43) with a known steady-state temperature 2977 K was placed at the in-focus distance from the lens on 10× magnification and imaged using the framing camera at various exposure times. This process yielded the 0–255 grayscale camera response (per pixel, per nanosecond of exposure) associated with a blackbody radiating at 2977 K at the location of the foil load, which was found to be 0.33 ns^{-1}. Blackbody spectra at temperatures from 2000 to 10 000 K were convolved with the wavelength-dependent camera response curves and integrated over the wavelength to give proportional values of the camera response as a function of temperature. The absolute calibration of camera response as a function of blackbody emitter temperature was obtained by normalizing the proportional camera response to 0.33 ns^{-1} at 2977 K and 10× magnification. This calibration was extended to other magnifications through the following relation:

$$\frac{R}{R_{10}} = \left(\frac{10}{m}\right)^2 \left(\frac{D}{D_{10}}\right)^2 \tag{8}$$

where R is the camera response on the 0–255 scale for a given temperature, R_{10} is the camera response for 10× magnification for the same temperature, m is the magnification, D is the in-focus distance at magnification m, and D_{10} is the in-focus distance for 10× magnification. In (8), the $(10/m)^2$ factor accounts for the increased collection area per pixel at lower magnifications and the $(D/D_{10})^2$ factor is due to the inverse square relationship with distance. In general, the temperature range that can be reliably measured by the camera varies from shot to shot as the camera response depends on both the exposure time and magnification; the minima and maxima are set by the temperatures corresponding to responses of 10 (the noise floor) and 245 (approaching saturation, above which the camera response is nonlinear with incident power). The camera response varied on the order of 5%–10% from frame to frame on the constant temperature calibration source, which places an approximated ±5% uncertainty on these temperature measurements obtained from the camera response.

To correlate the camera response with an emitting surface temperature of an ablating aluminum foil, the emissivity of aluminum in the temperature range of interest is also required. While the emissivity of solid and liquid aluminum has been experimentally measured at temperatures below 1500 K [32], little information exists on the aluminum emissivity at temperatures in the 2000–10 000 K range. For this paper, the emissivity ϵ_{Al} of both biphase liquid/vapor aluminum at the vaporization point and superheated aluminum vapor was assumed to be 1. This assumption places a lower bound on the temperature of the emitting regions. For comparison, the difference in temperature calculated using $\epsilon_{Al} = 1$ compared with $\epsilon = 0.4$ (the typical of refractory metals near their ∼3000 K melting points) is around 25%, while the difference compared with $\epsilon \sim 0.1$ (the characteristic of liquid aluminum above 1000 K) is around 50%. While these errors are significantly larger than the ±5% error due to the camera response uncertainty, it is noteworthy that measurements using this temperature inversion technique of partially vaporized biphase aluminum with an expected temperature equal to T_{vapor} (2743 K, the atmospheric pressure vaporization temperature of aluminum) yielded values centered around 2700 K. These measurements are discussed in detail in Section IV. We make the following two observations on the accuracy of the measurement technique: 1) the intrinsic camera response error places a ±5% uncertainty on the *lower bound* of position-dependent temperature measurements and 2) the uncertainty *with respect to the lower bound* may be as high as 50% due to the unknown emissivity of very hot aluminum, but our experimental evidence suggests that this second uncertainty may be much lower in practice.

IV. Experimental Observations of Temperature Perturbations

Image sequences of ablating foils were converted into temperature data using the response calibrations described in the previous section. A total of 102 shots were conducted in ambient air over the current density parameter space of interest. While the framing camera was timed too early or too late relative to start-of-current to capture the onset of resolvable light emission on some shots, the formation of hot perpendicular-to-current striations was observed without exception for shots with good camera timing (∼60 out of the 102 total shots). Fig. 4 shows a typical temperature measurement sequence for the central 1.25 mm × 1.08 mm region of an 800-nm thick, 10-mm-wide foil, demonstrating the formation of striations arising from merging of initial hotspots. Temperature measurements presented in this section represent the lower bounds calculated from the camera response assuming $\epsilon = 1$. As described in Section III, the exposure time and pixel size of each image establishes a resolvable temperature range, above which the camera reads saturation and below which the camera reads below the noise floor of response.

Comparing the time integral of the power deposited in the foil (as measured from the voltage and current data) with the total energy required to vaporize the foil from room temperature revealed that the bright filamentary structures consistently occurred before the bulk foil had vaporized. During the formation and development of the bright striations, the energy deposited in the foil divided by the foil mass was larger than the quantity q_1, the integral of the specific heat from room temperature to boiling temperature plus the latent heat of fusion, but smaller than q_2, the latent heat of vaporization plus q_1. Moreover, for all but the smallest cross section foils, the stored energy in the capacitor bank divided by the foil mass was lower than q_2 (but significantly higher than q_1). As these bright spots correspond to temperature measurements significantly hotter than the vaporization temperature of aluminum—thousands of kelvins hotter in some cases—this observation indicates the existence of a significant spatial heterogeneity in energy deposition prior to the bulk foil explosion.

Because the time frame of interest for each shot uniformly occurred after the bulk foil had received sufficient energy

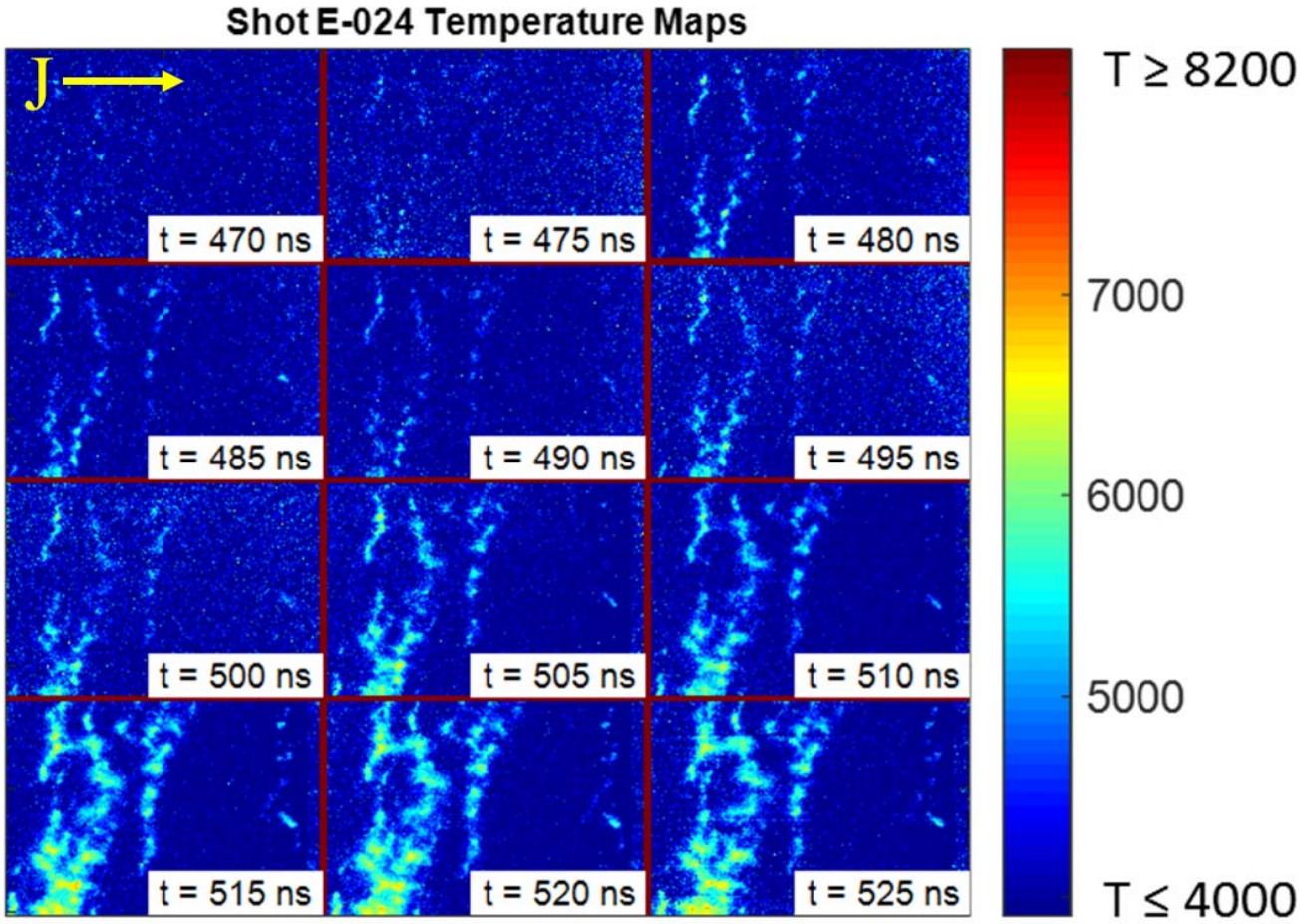

Fig. 4. Temperature surface maps (in Kelvin) for an 800 nm × 1.0 cm × 0.9 cm foil; average current density over the observation window was 3.9×10^7 A/cm^2. Image sizes are 1.08 mm × 1.25 mm, current flows from left to right. Temperatures outside the range of 4000–8200 K are unresolvable because they are outside of the boundaries set by the noise floor and saturation limits of the camera. Temperatures above the 4000-K noise floor represent a lower bound due to the $\epsilon = 1$ assumption with uncertainty on this lower bound of ±5%.

to reach the vaporization temperature but before enough energy had been deposited to overcome the latent heat of vaporization, it was anticipated that the unperturbed aluminum should be in the biphase liquid–vapor transition at these times. The "dark" regions of framing camera images are therefore expected to correspond to the vaporization temperature of aluminum at atmospheric pressure T_{vapor} (2743 K). To verify this assumption, several shots were performed with long (40–80 ns) exposure times to resolve these relatively low temperatures at the cost of temporal resolution (see Fig. 5).

Fig. 5 shows striations beginning to form with the hottest spots already exceeding the maximum resolvable temperature of 4200 K. Far from these striations, the temperature of the material is in the 2600–2800 K range, showing an excellent agreement with the predicted 2743 K. For all shots with a higher resolvable temperature floor, such as the shot shown in Fig. 5, the bulk foil material is therefore assumed to be at $T_b = T_{\text{vapor}}$. The hot bright striations are then taken to be perturbations in temperature superimposed on the bulk biphase aluminum. Setting the average temperature of the foil equal to T_{vapor} inherently assumes that the mass contained in the hot striations is small compared to the total mass of the foil. This assumption is reasonable because the deposited energy, which has already been established as insufficient to bulk vaporize the foil during the time frame of interest,

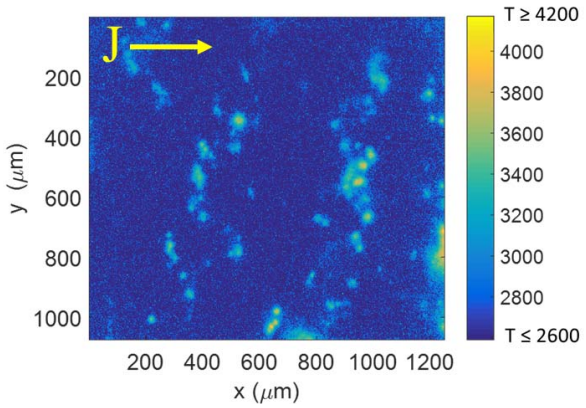

Fig. 5. Temperature plot (in Kelvin) of an 80-ns exposure image, taken on an 800 nm × 1.0 cm × 0.9 cm aluminum foil to establish the temperature of the background aluminum (which is always below the noise floor on shorter exposure images). For this exposure and magnification, resolvable temperature range is 2600–4200 K. Temperatures above the noise floor represent a lower bound due to the $\epsilon = 1$ assumption with uncertainty on this lower bound of ±5%.

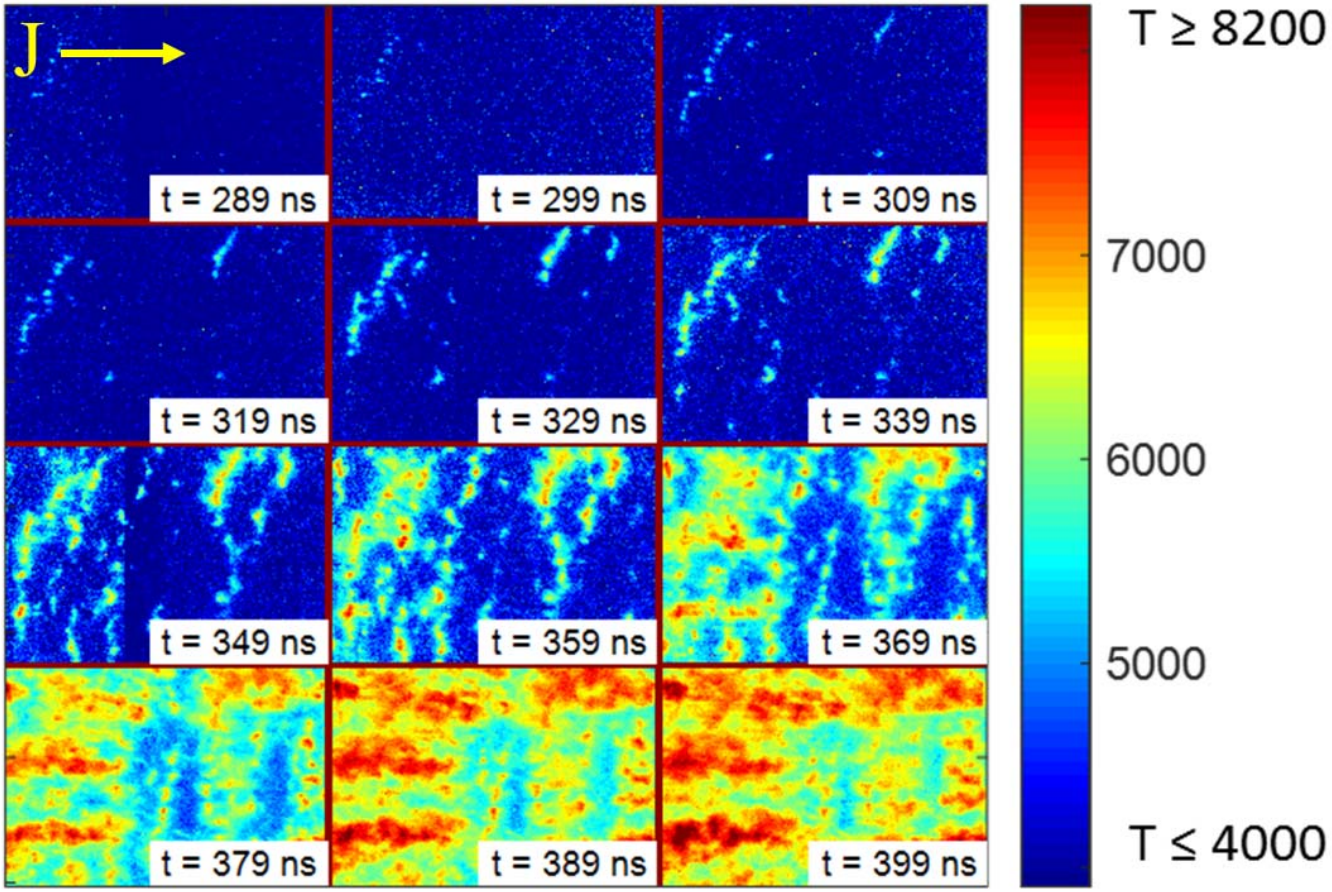

Fig. 6. Temperature surface plot of an 800 nm × 0.7 cm × 0.9 cm aluminum foil ablation showing plasma from vaporized sections of the foil merging and developing filamentary (parallel-to-current) structures late in time. Image sizes are 1.08 mm × 1.25 mm, current flows from left to right. Temperatures above the noise floor represent a lower bound due to the $\epsilon = 1$ assumption with uncertainty on this lower bound of ±5%.

was certainly insufficient to raise a sizeable fraction of the material to temperatures greatly exceeding the vaporization temperature.

Structures parallel to the direction of the current, believed to be the filamentation form of ETI, were also observed on several of the highest current density shots that included late-time images. These late frames showed plasma features that began to merge and form filaments above the surface of the bulk material. Fig. 6 presents a typical temperature surface plot sequence showing this phenomenon.

Although the later frames of Fig. 6 appear to be completely covered in hot plasma, sufficient energy had not been delivered to the foil to vaporize the bulk material by the last frame. This is possibly explained by a continuing runaway heating process in zones which had already vaporized due to ETI owing to the additional effects of the density dependence of resistivity. Further heating of vaporized striations may be sufficient to cause ionization and the transition to a Spitzer-like, negative $\partial\eta/\partial T$ regime above the surface of the background aluminum (which is still biphase liquid/vapor at T_{vapor}). This top layer of plasma would then be expected to be unstable to filamentation-form ETI. A future computational study may be warranted to investigate this phenomenon further.

In general, the merging of initial hotspots to form perpendicular-to-current striations appeared to be a random process. As the initial foils were known to contain both surface deformations (wrinkles) and impurity inclusions, a series of six shots was performed to probe the relative contribution to ETI formation due to the two types of imperfections. For the first three shots, a standard #0-80 screw was rolled onto strips of the 800-nm aluminum foil to impress grooves approximately 320 μm apart that dominated the natural folds in the foil. These grooves were impressed at 70° relative to the direction of current flow to minimize the chance of confusing randomly occurring perpendicular-to-current structures with structures seeded by the grooves; this 70° angle is well above the minimum growing angular condition for striation-form ETI given by (3). A groove-seeded foil and the associated temperature measurement sequence are shown in Fig. 7. Fig. 7 demonstrates a lack of correlation between the initial surface perturbations and ETI that develops; this result was consistent with the other shots taken with the same initial conditions.

To mimic the effect of resistive inclusion seeding, three additional shots were conducted on foils that had two holes of approximately 50-μm-diameter machined ~1 cm apart. These holes were positioned such that the line joining them

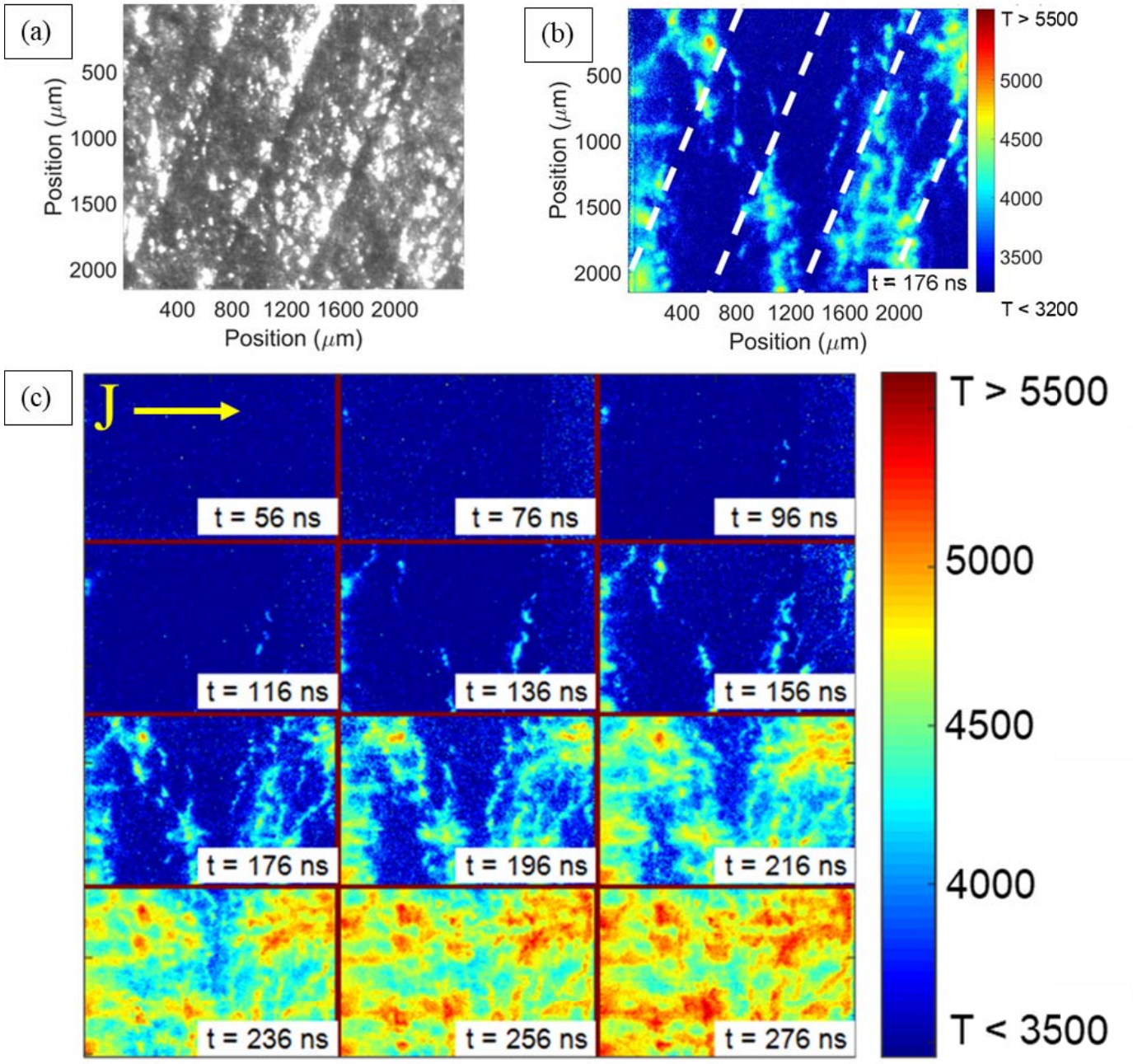

Fig. 7. (a) Preshot image showing grooves embedded in an 800 nm × 0.7 cm × 0.9 cm foil to impose a long-wavelength surface deformation. Grooves are approximately 320 μm apart. (b) Selected image around the formation time of the first striations. White lines: location of the initial temperature grooves. (c) Full temperature plot sequence showing instability growth. All image sizes are 2.5 mm × 2.15 mm; current flows from left to right. Temperatures above the noise floor represent a lower bound due to the $\epsilon = 1$ assumption with uncertainty on this lower bound of ±5%.

was approximately 75° from the parallel-to-current direction. Because one of the primary impurities in the aluminum foils used throughout this paper is silicon (which has a room temperature resistivity that is 7 to 8 orders of magnitude higher than aluminum), the holes were taken to be a good approximation of a large silicon inclusion. Fig. 8 shows the typical results from a shot with the machined holes.

A clear ETI striation can be seen in Fig. 8(b), joining the position of the holes shown in Fig. 8(a). This provides experimental confirmation of the self-correlation of ETI around a resistive hotspot as proposed conceptually in Fig. 1. Fig. 8(c) shows that the seeded structure is the first ETI striation to form and is dominant up until most of the striations have expanded and merged. This observation may indicate the physical mechanism responsible for the previously observed reduction in the density of ETI striations with increasing material purity [28].

V. Analysis of Striation-Form ETI Growth Rates

To compare the experimental data with theoretical predictions of ETI growth rate, a procedure was established to

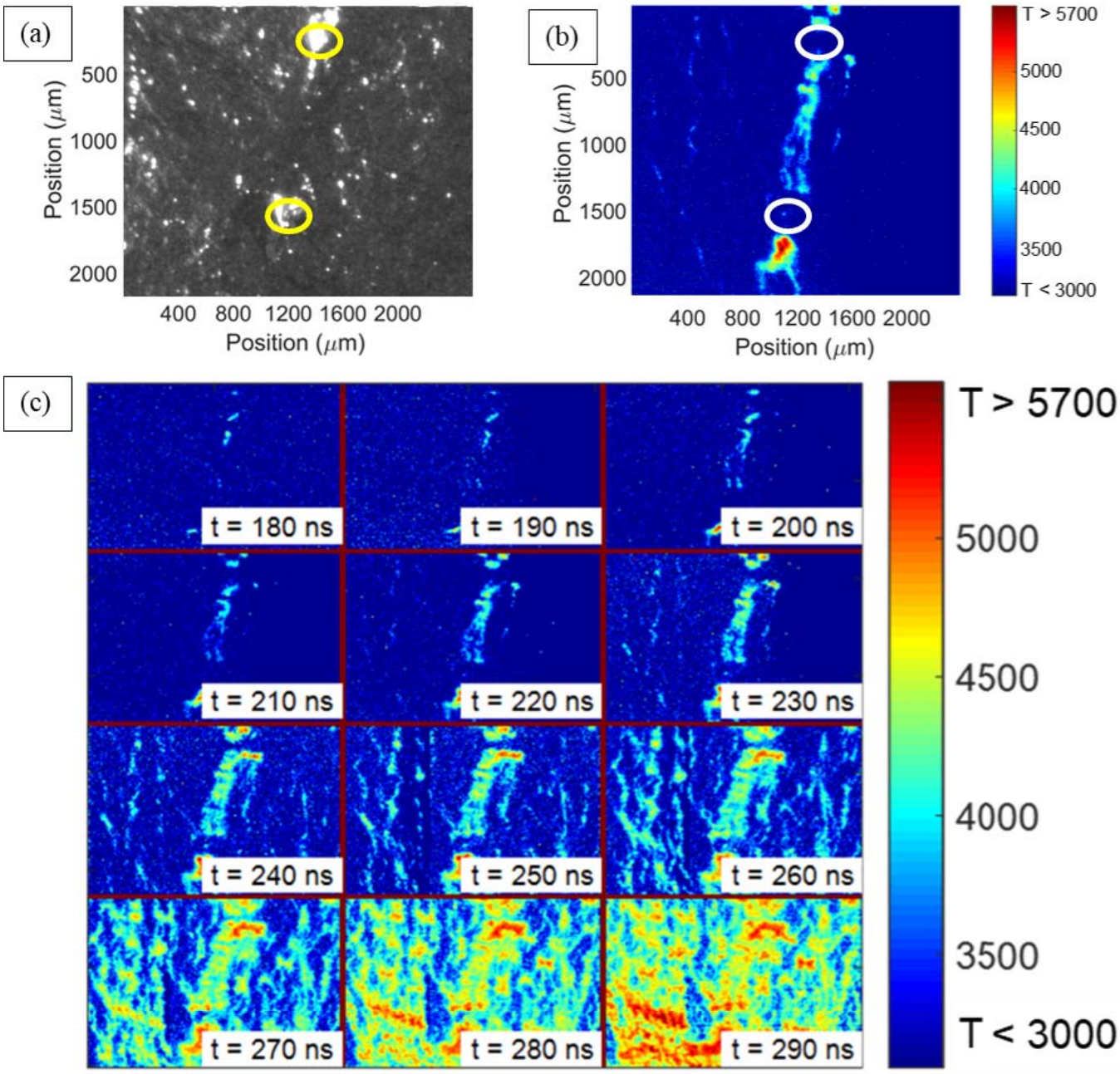

Fig. 8. (a) Preshot image showing two holes (yellow circles) with diameter ~ 50 μm punctured in a 400 nm $\times$ 1.0 cm $\times$ 0.9 cm foil to approximate large inclusions of high-resistivity impurities. (b) Temperature plot generated from image taken at 220 ns showing ETI preferentially forming along the line between the holes (white circles) before growing elsewhere along the foil. (c) Full shot temperature sequence. Note the seeded striation begins to grow $\sim$50 ns prior to random striations. All image sizes are 2.5 mm $\times$ 2.15 mm; current flows from left to right. Temperatures above the noise floor represent a lower bound due to the $\epsilon = 1$ assumption with uncertainty on this lower bound of $\pm 5\%$.

determine a temporally and spatially averaged growth rate for the observation window of a given shot. For each of the 12 temperature map images in a shot sequence, a 10 $\times$ 1-pixel binning algorithm was applied in the perpendicular-to-current direction (vertical on the images) to locally average the signal, reducing each original 860 $\times$ 1000-pixel image to 86 horizontal lineouts. This binning process reduces the impact of individual saturated pixels that appeared in small numbers on all camera images due to noise while still preserving resolution in the parallel-to-current (horizontal) direction. Two example lineouts from an 800 nm $\times$ 0.7 cm $\times$ 0.9 cm foil are shown in Fig. 9(a) and (b).

Of the 102 total shots, 13 were identified with all 12 images taking place during the growing temperature perturbation phase on all frames (i.e., no all-black or all-saturated frames in the sequence) and selected for growth rate analysis. As described in Section IV, the unperturbed bulk temperature was assumed to be T_{vapor}, 2743 K. To measure the growth rate, temperature peaks are extracted from lineouts, and the measured, lower bound temperature of each peak T_{peak} is

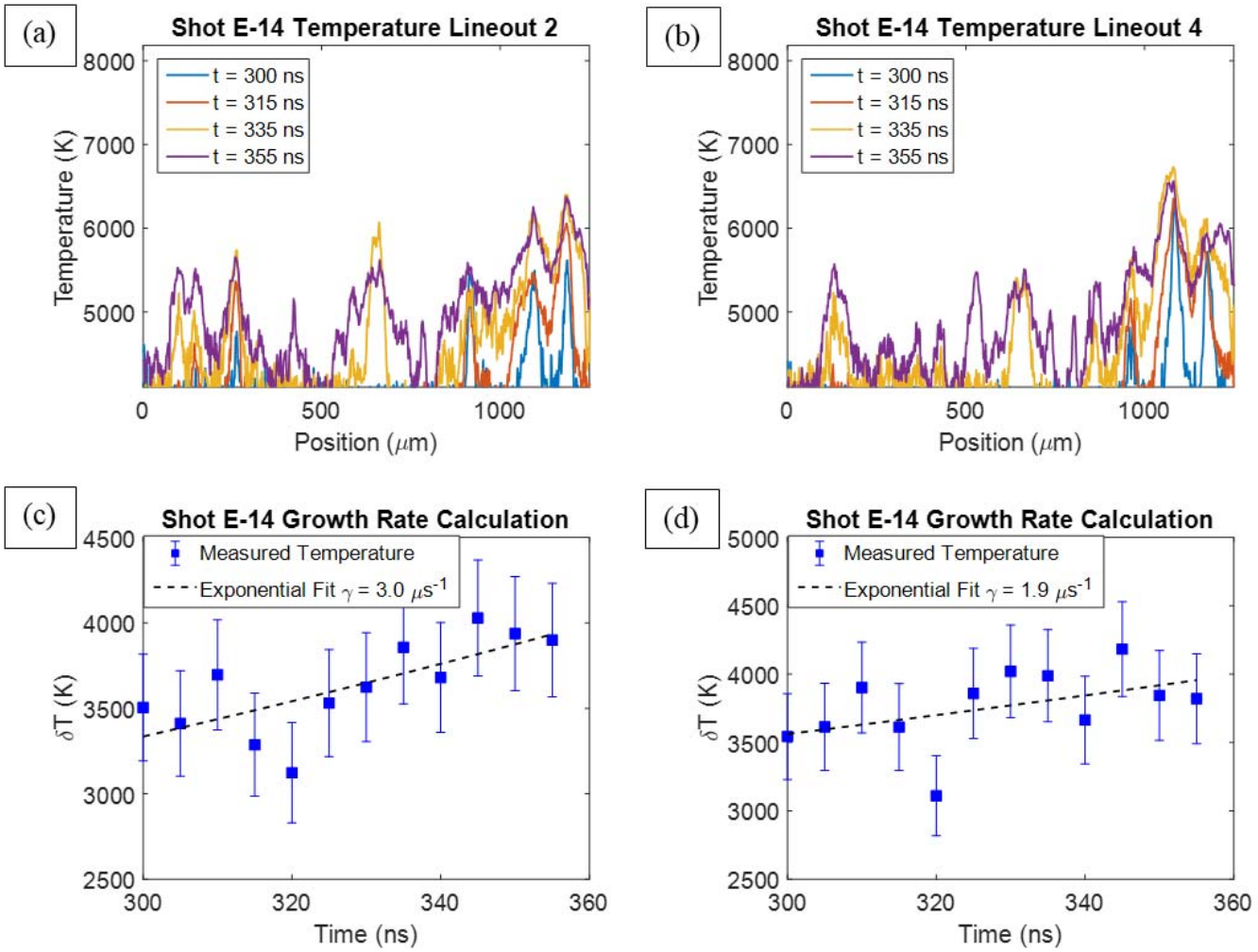

Fig. 9. (a) and (b) Example temperature lineouts (2 lineouts of the total 86 obtained from the shot; 4 of the available 12 frames are shown per lineout) from an 800 nm × 0.7 cm × 0.9 cm foil ablation. The y-axes are truncated at 4000 K because temperatures below this value cannot be resolved for the specified magnification and exposure time. (c) and (d) Corresponding growth rate plots from the highest temperature points on each temperature lineout. Error bars: frame-to-frame ±5% response error of the camera.

plotted as a function of time over the 12 frames. The growth rate for a given peak is determined by fitting a linear function to the natural logarithm of δT, where $\delta T(t) = T_{\text{peak}}(t) - T_{\text{vapor}}$ [see Fig. 9(c) and (d)]. All values of the growth rate calculated in this manner for a given shot are averaged to give a characteristic growth rate for that shot (downselected to exclude peaks that saturate the camera on later frames; at a minimum 25 growth rates were averaged per shot). Uncertainty on each growth rate lineout σ_{growth} is taken to be the 95% confidence interval on the fit of $\ln(\delta T)$ versus T, with σ_{growth} represented as a fraction of the measured growth rate. The total uncertainty in the growth rate for a given shot is then approximated by $\Sigma_n|\sigma_{\text{growth}}|/(n\sqrt{n})$, where n is the number of lineouts used in the averaging process.

The linear theoretical growth rate of striation-form ETI given by (4) depends on both time and temperature. In addition, η, c_v, κ, and ρ vary as a function of temperature within a single phase and as deposited energy during the constant-temperature vaporization process. To determine the time-dependent theoretical growth rate, the average temperature of the foil and enthalpy change from room temperature during the vaporization phase change were tracked as a function of time for each shot using the input power measurements. Values of η, c_v, κ, and ρ are interpolated as functions of temperature and/or enthalpy from the available data in the literature [21]–[26], under the assumption that these values are weak functions of pressure. Theoretical ETI growth rates are then calculated, as functions of time, for wavenumber k ranging from $k = 10^6$ m^{-1} (near the minimum experimentally resolvable wavelength) to $k = 10^4$ m^{-1} (a large enough wavelength such that $\gamma > 0.99\gamma_{\max}$), using the input energy measured for each shot. The measured temporally and spatially averaged growth rate is then compared to theoretical ETI growth rates over the observation window. Fig. 10 shows an example growth rate comparison, with the measured average growth rate indicated by the dashed black line; the calculated, time-dependent growth rates for various ETI wavelengths indicated by the colored curves; and the observation window of the 12-frame ICCD indicated by the shaded box.

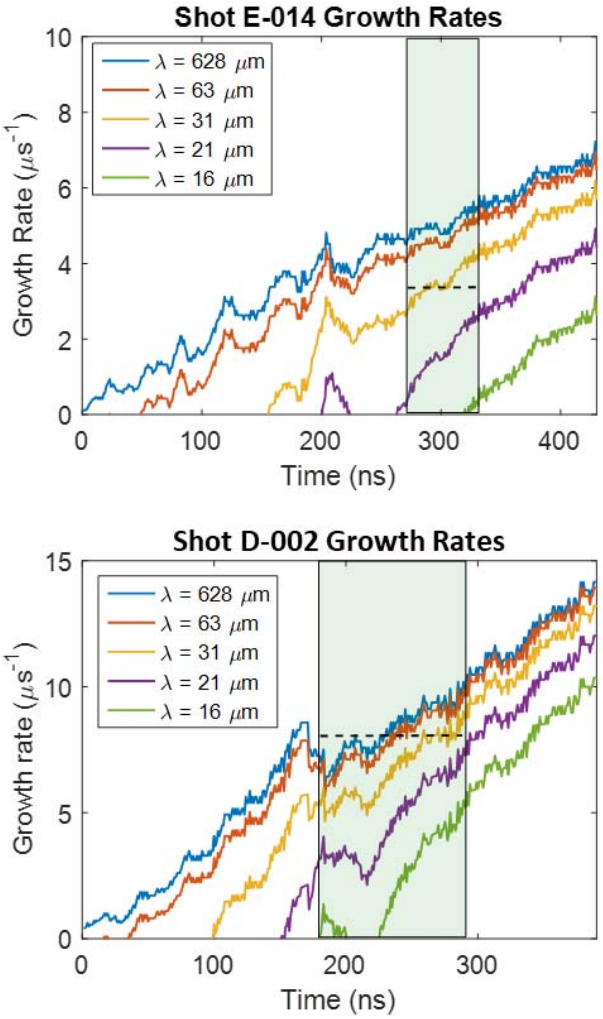

Fig. 10. Example time-dependent growth rates $\gamma(t, T, k)$ calculated from (4) with the imaging window indicated as a shaded box. The measured average growth rate is shown as a dashed horizontal line to compare with the theoretical values. Blue (top) curve is approximately indicative of $\gamma_{\max}$ as its corresponding wavelength is two orders of magnitude greater than $\lambda_{\min}$.

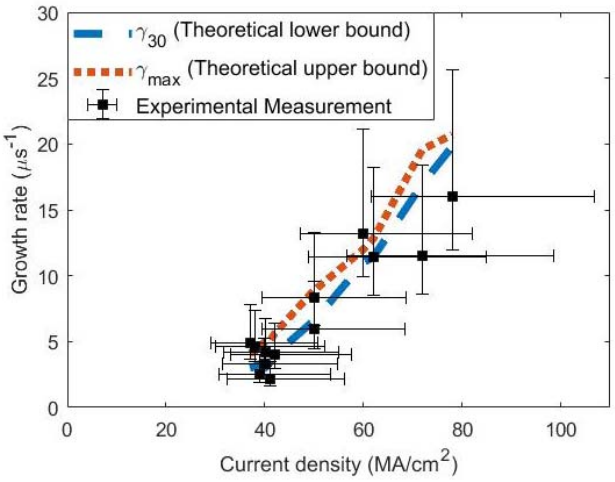

Fig. 11. Measured ETI growth rates plotted as a function of current density. Theoretical growth rates calculated from corresponding current and voltage measurements are shown as dashed lines for $\gamma_{\max}$ (top line) and γ_{30} (bottom line). These curves represent the maximum and minimum growth expected from ETI theory for wavelengths observed on the experimental data. Horizontal error bars: uncertainty in current density due to the uncertainty in foil width and thickness. Vertical error bars: uncertainty from the averaged growth rate fits to experimental δT data.

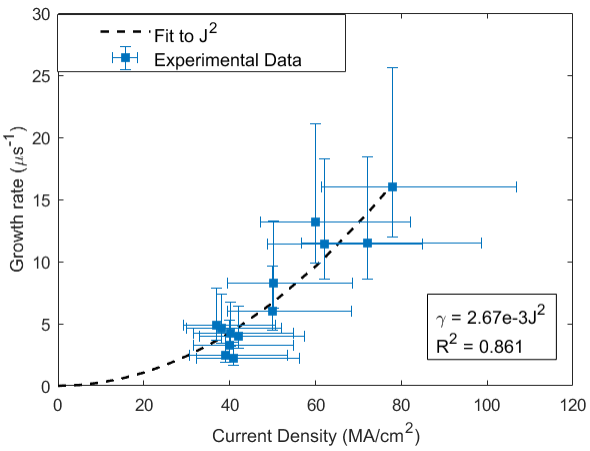

Fig. 12. Experimentally measured growth rates from Fig. 11 plotted against current density.

Fig. 10 shows the measured average growth rates in reasonably good agreement with calculated ETI growth rates in the range of $\lambda = 30\ \mu$m, the smallest experimentally observed growing wavelength across all shots, to $\gamma = 628\mu$m, taken to be a "very large" perturbation. A very large perturbation grows as $\gamma_{\max}$, the maximum theoretical growth rate for a given current density and material, defined in (5). Generally, measured average growth rates were found to fall within or close to the range bounded by the calculated growth rates γ_{30} (the growth rate for $\lambda = 30\ \mu$m) and $\gamma_{\max}$. The growth rate results from all 13 analyzed shots are summarized in Fig. 11.

From Fig. 11, measured growth rates from five out of the 13 shots fall in the window bounded by γ_{30} and $\gamma_{\max}$, and the remaining measured growth rates fall within 50% of these theoretical upper and lower bounds. It is noteworthy that $\delta T/T_{\text{vapor}}$ exceeded unity for most of these experiments, so it is somewhat surprising that the experimental data show a degree of quantitative agreement with the linear theory. This agreement is even more remarkable when considering: 1) the sources of error, which include the ±27% error on the current density and ±5% error on the camera response and 2) the assumptions that the background aluminum is expansionless and that its properties can be approximated as pressure independent.

As discussed in Section II, the growth rate $\gamma_{\max}$ of long-wavelength ETI is anticipated to scale with the square of current density; additionally, the growth rate of long-wavelength ETI with zero current density should be zero. Because the majority of observed perturbations had long wavelengths on the order of 100s of μm, measured growth rates are expected to scale approximately quadratically with J. Fig. 12 shows the measured growth rates plotted as a function of current density with a least-squares curve fit to J^2.

The data shown in Fig. 12 are reasonably well characterized by a quadratic dependence on J^2. The least-squares best fit

proportionality constant was found to be 2.7×10^{-17} $m^4/(A^2 \cdot s)$, with a 95% confidence interval of 1.1×10^{-17} $m^4/(A^2 \cdot s)$ to 4.3×10^{-17} $m^4/(A^2 \cdot s)$. This is consistent with the theoretically predicted value, 3.8×10^{-17} $m^4/(A^2 \cdot s)$, which is the ratio $(\partial\eta/\partial T)/(\rho c_v)$ for liquid aluminum at the vaporization temperature [21]–[26]. The consistency between experimental measurements and theoretical prediction demonstrated in Figs. 10–12 provide significant evidence that the growing temperature perturbations observed on the ablating foils are in fact manifestations of the striation form of ETI.

VI. Conclusion

Pulsed power ablations of thin metallic foils were carried out to investigate the growth of ETI over a range of current densities. A temperature diagnostic was developed using a 12-frame ultrafast ICCD to provide time-resolved measurements of temperature perturbations on the foil surfaces. The experimentally observed temperature perturbations exhibited four key phenomena consistent with the theoretical understanding of ETI: 1) temperature perturbations in the perpendicular-to-current orientation self-correlated and grew exponentially with rates in good agreement with theoretical striation-form ETI growth; 2) the growth rate of large wavelengths scaled approximately as the square of current density; 3) the seeding of perturbations depended more strongly on high-resistivity inclusions than the deformation of the foil surface; and 4) temperature perturbations transitioned from a perpendicular-to-current orientation to a parallel-to-current orientation at times much later than the start of visible light emission. These findings agree well with the previous experimental study of ETI [13], [28] and provide strong experimental evidence of the growth of striation-form ETI on pulsed power ablations of electrically thin, initially solid metal loads. The experimental validation of ETI theory motivates ongoing campaigns to reduce ETI on pulsed power ablation experiments and thereby delay the formation of destructive plasma instabilities.

Acknowledgment

The authors would like to thank Dr. S. Patel for assistance with spectroscopic measurements and Dr. T. Awe for useful conversations regarding ETI research at Sandia National Laboratories.

References

[1] J. E. Bailey *et al.*, "Dynamic hohlraum radiation hydrodynamics," *Phys. Plasmas*, vol. 13, no. 5, p. 056301, 2006.
[2] G. A. Rochau *et al.*, "High performance capsule implosions driven by the Z-pinch dynamic hohlraum," *Plasma Phys. Controlled Fusion*, vol. 49, no. 12B, p. 591, 2007.
[3] M. D. Knudson, D. L. Hanson, J. E. Bailey, C. A. Hall, J. R. Asay, and C. Deeney, "Principal Hugoniot, reverberating wave, and mechanical reshock measurements of liquid deuterium to 400 GPa using plate impact techniques," *Phys. Rev. B, Condens. Matter*, vol. 69, p. 144209, Apr. 2004.
[4] R. E. Reinovsky, "Instability growth in magnetically imploded high-conductivity cylindrical liners with material strength," *IEEE Trans. Plasma Sci.*, vol. 30, no. 5, pp. 1764–1776, Oct. 2002.
[5] J. E. Bailey *et al.*, "A higher-than-predicted measurement of iron opacity at solar interior temperatures," *Nature*, vol. 517, pp. 56–59, Jan. 2015.
[6] M. R. Martin *et al.*, "Solid liner implosions on Z for producing multi-megabar, shockless compressions," *Phys. Plasmas*, vol. 19, no. 5, p. 056310, 2012.
[7] S. A. Slutz *et al.*, "Pulsed-power-driven cylindrical liner implosions of laser preheated fuel magnetized with an axial field," *Phys. Plasmas*, vol. 17, no. 5, p. 056303, 2010.
[8] S. A. Slutz and R. A. Vesey, "High-gain magnetized inertial fusion," *Phys. Rev. Lett.*, vol. 108, p. 025003, Jan. 2012.
[9] M. E. Cuneo *et al.*, "Magnetically driven implosions for inertial confinement fusion at Sandia National Laboratories," *IEEE Trans. Plasma Sci.*, vol. 40, no. 12, pp. 3222–3245, Dec. 2012.
[10] A. B. Sefkow *et al.*, "Design of magnetized liner inertial fusion experiments using the Z facility," *Phys. Plasmas*, vol. 21, no. 7, p. 072711, 2014.
[11] M. R. Gomez *et al.*, "Experimental demonstration of fusion-relevant conditions in magnetized liner inertial fusion," *Phys. Rev. Lett.*, vol. 113, p. 155003, Oct. 2014.
[12] M. R. Weis *et al.*, "Coupling of sausage, kink, and magneto-Rayleigh-Taylor instabilities in a cylindrical liner," *Phys. plasmas*, vol. 22, p. 032706, Mar. 2015.
[13] K. J. Peterson *et al.*, "Electrothermal instability growth in magnetically driven pulsed power liners," *Phys. Plasmas*, vol. 19, p. 092701, Aug. 2012.
[14] K. J. Peterson *et al.*, "Simulations of electrothermal instability growth in solid aluminum rods," *Phys. Plasmas*, vol. 20, p. 056305, Feb. 2013.
[15] K. J. Peterson *et al.*, "Electrothermal instability mitigation by using thick dielectric coatings on magnetically imploded conductors," *Phys. Rev. Lett.*, vol. 112, p. 135002, Apr. 2014.
[16] T. J. Awe *et al.*, "Experimental demonstration of the stabilizing effect of dielectric coatings on magnetically accelerated imploding metallic liners," *Phys. Rev. Lett.*, vol. 116, p. 065001, Feb. 2016.
[17] A. M. Steiner *et al.*, "The electro-thermal stability of tantalum relative to aluminum and titanium in cylindrical liner ablation experiments at 550 kA," *Phys. Plasmas*, vol. 25, p. 032701, Feb. 2018.
[18] D. D. Ryutov, M. S. Derzon, and M. K. Matzen, "The physics of fast *Z* pinches," *Rev. Mod. Phys.*, vol. 72, no. 1, p. 167, 2000.
[19] D. A. Yager-Elorriaga *et al.*, "Discrete helical modes in imploding and exploding cylindrical, magnetized liners," *Phys. Plasmas*, vol. 23, p. 124502, Nov. 2016.
[20] D. A. Yager-Elorriaga, P. Zhang, A. M. Steiner, N. M. Jordan, Y. Y. Lau, and R. M. Gilgenbach, "Seeded and unseeded helical modes in magnetized, non-imploding cylindrical liner-plasmas," *Phys. Plasmas*, vol. 23, p. 101205, Aug. 2016.
[21] G. R. Gathers, "Thermophysical properties of liquid copper and aluminum," *Int. J. Thermophys.*, vol. 4, no. 3, pp. 209–226, 1983.
[22] E. H. Buyco and F. E. Davis, "Specific heat of aluminum from zero to its melting temperature and beyond. Equation for representation of the specific heat of solids," *J. Chem. Eng. Data*, vol. 15, no. 4, pp. 518–523, 1970.
[23] P. D. Desai, T. K. Chu, H. M. James, and C. Y. Ho, "Electrical resistivity of selected elements," *J. Phys. Chem. Reference Data*, vol. 13, p. 1069, Oct. 2009.
[24] E. A. Brandes and G. B. Brook, *Smithells Metals Reference Book*, 7th ed. Oxford, U.K.: Butterworth-Heinemann, 1992.
[25] B. Giordanengo, N. Benazzi, J. Vinckel, J. G. Gasser, and L. Roubi, "Thermal conductivity of liquid metals and metallic alloys," *J. Non-Crystalline Solids*, vols. 250–252, pp. 377–383, Aug. 1999.
[26] D. H. Menzel, *Fundamental Formulas of Physics*, 2nd ed. New York, NY, USA: Dover, 2011.
[27] V. I. Oreshkin, "Thermal Instability during an electrical wire explosion," *Phys. Plasmas*, vol. 15, p. 092103, Jul. 2008.
[28] T. J. Awe *et al.*, "On the evolution from micrometer-scale inhomogeneity to global overheated structure during the intense joule heating of a z-pinch rod," *IEEE Trans. Plasma Sci.*, vol. 45, no. 4, pp. 584–589, Apr. 2017.
[29] A. M. Steiner, "The electrothermal instability on pulsed power ablations of thin foils," Ph.D. dissertation, Univ. Michigan, Ann Arbor, MI, USA, 2016.
[30] H. W. Liepmann and A. Roshko, *Elements of Gasdynamics*. New York, NY, USA: Wiley, 1957.
[31] Y. B. Zel'dovich and Y. P. Raizer, *Physics of Shock Waves and High-Temperature Hydrodynamic Phenomena*. New York, NY, USA: Academic, 1966.
[32] S. Krishnan and P. C. Nordine, "Optical properties of liquid aluminum in the energy range 1.2–3.5 eV," *Phys. Rev. B, Condens. Matter*, vol. 47, no. 18, pp. 11780–11787, 1993.

Adam M. Steiner (S'10–M'17) received the B.S. degree in nuclear engineering and physics from North Carolina State University, Raleigh, NC, USA, in 2010, and the M.S. and Ph.D. degrees in nuclear engineering from the University of Michigan, Ann Arbor, MI, USA, in 2012 and 2016, respectively.

He is currently a Senior Electrical Engineer with the Skunk Works Team, Lockheed Martin Aeronautics Company, Palmdale, CA, USA. He has been involved in pulsed power driver development for high-density plasma sources and large magnetic field generation from high-temperature superconductors.

Paul C. Campbell (S'16), photograph and biography not available at the time of publication.

David A. Yager-Elorriaga (S'13–M'17), photograph and biography not available at the time of publication.

Nicholas M. Jordan (S'05–M'13) received the B.S.E., M.S.E., and Ph.D. degrees in nuclear engineering (with a minor in plasma physics) from the University of Michigan (UM), Ann Arbor, MI, USA, in 2002, 2004, and 2008, respectively.

He was with Cybernet Systems, Ann Arbor, MI, USA, where he was involved in microwave vehicle stopping technology. In 2013, he was an Assistant Research Scientist with the Plasma, Pulsed Power, and Microwave Laboratory, UM. His current research interests include high-power microwave devices, pulsed power, laser ablation, Z-pinch physics, and plasma discharges.

Ryan D. McBride (M'00) received the Ph.D. degree from Cornell University, Ithaca, NY, USA, in 2009, with a focus on wire-array z-pinch implosions using the 1-MA COBRA pulsed power facility.

From 2008 to 2016, he was a Staff Physicist and a Department Manager with the Sandia National Laboratories, Albuquerque, NM, USA, where he was involved in nuclear fusion, radiation generation, and high-pressure material properties using the 25-MA Z pulsed power facility. He is currently an Associate Professor with the Department of Nuclear Engineering and Radiological Sciences, University of Michigan, Ann Arbor, MI, USA, where he is with the Plasma, Pulsed Power, and Microwave Laboratory, which includes two linear transformer driver facilities: MAIZE (∼1 MA, ∼100 ns) and BLUE (∼150 kA, ∼100 ns). He is currently involved in both experimental and theoretical studies of magnetized liner inertial fusion (MagLIF). His current research interests include plasma physics, nuclear fusion, radiation generation, pulsed power technology, plasma diagnostics, and the dynamics of magnetically driven, cylindrically imploding systems.

Y. Y. Lau (M'98–SM'06–F'08) received the B.S., M.S., and Ph.D. degrees in electrical engineering from the Massachusetts Institute of Technology, Cambridge, MA, USA, in 1968, 1970, and 1973, respectively.

He is currently a Professor with the Department of Nuclear Engineering and Radiological Sciences, University of Michigan, Ann Abor, MI, USA. He is involved in electron beams, coherent radiation sources, plasmas, and discharges. He has authored or co-authored more than 250 refereed publications. He holds 11 patents. His current research interests include electrical contacts, heating phenomenology, high-power microwave sources, and magneto-Rayleigh–Taylor instabilities.

Dr. Lau is a Fellow of the American Physical Society in 1986. He was a recipient of the 1999 IEEE Plasma Science and Applications Award and the 2017 IEEE John R. Pierce Award for Excellence in Vacuum Electronics. He served three terms as an Associate Editor for Physics of Plasmas from 1994 to 2005.

Ronald M. Gilgenbach (M'74–F'06–LF'15) received the B.S. and M.S. degrees from the University of Wisconsin–Madison, Madison, WI, USA, and the Ph.D. degree in electrical engineering from Columbia University, New York, NY, USA, in 1978.

In 1970, he was a Technical Staff Member with the Bell Telephone Labs., Holmdel, NJ, USA. From 1978 to 1980, he was with the Naval Research Laboratory, Washington, DC, USA. He was with the Oak Ridge National Laboratory, Oak Ridge, TN, USA, where he performed the first electron cyclotron heating experiments on a tokamak plasma. He joined the faculty of the University of Michigan (UM), Ann Abor, MI, USA, in 1980 and the Founder of the Plasma, Pulsed Power, and Microwave Laboratory. He has supervised 50 graduated Ph.D. students. He is currently a Chihiro Kikuchi Collegiate Professor with the Nuclear Engineering and Radiological Sciences Department, UM.

Dr. Gilgenbach is a Fellow of the American Physical Society, the Division of Plasma Physics, and the American Nuclear Society. He was a recipient of the 1997 IEEE Plasma Sciences and Applications Committee Award and the 2017 IEEE Peter Haas Pulsed Power Award. He served as the IEEE PSAC Chair from 2007 to 2008. He was an Associate Editor of *Physics of Plasmas*.